[*Reprinted from* THE AERONAUTICAL JOURNAL OF THE ROYAL AERONAUTICAL SOCIETY, *MAY 1997*]

UH-60A helicopter rotor airloads measured in flight

R. M. Kufeld
Aerospace Engineer,
Nasa Ames Research Center,
Moffett Field, California, USA

W. G. Bousman
Research Scientist,
US Army Aeroflightdynamics Directorate (Atcom),
Moffett Field, California, USA

PRINTED BY MANOR PARK PRESS LIMITED, EDISON ROAD, HAMPDEN PARK, EASTBOURNE, SUSSEX, ENGLAND
AND PUBLISHED BY THE ROYAL AERONAUTICAL SOCIETY, 4 HAMILTON PLACE, LONDON W1V 0BQ, ENGLAND

UH-60A helicopter rotor airloads measured in flight

R. M. Kufeld
Aerospace Engineer
Nasa Ames Research Center
Moffett Field, California, USA

W. G. Bousman
Research Scientist
US Army Aeroflightdynamics Directorate (Atcom)
Moffett Field, California, USA

ABSTRACT

The flight test phase of the Nasa–Army UH-60A Airloads Program was completed in February 1994. The objective of the project was to measure the airloads in flight on an UH-60A Black Hawk using 221 blade pressure transducers installed in nine radial arrays. In addition, 21 transducers were installed along the blade leading edge to better identify blade-vortex interaction phenomena. This paper briefly describes the program's background and history, instrumentation, and data acquisition. Airloads data are presented for two test conditions with different levels of complexity: steady, level flight and a diving turn. These flight data provide useful information of relatively simple and complex nonlinear flow for the validation of theoretical analyses. Evidence of shock waves, reverse flow, dynamic stall and blade vortex interactions are presented.

NOMENCLATURE

a	speed of sound, ft/s
b	number of blades
c	blade chord, ft
C_w/σ	weight coefficient, $\dfrac{GW}{\pi\sigma\rho\Omega^2R^4}$
GW	aircraft gross weight, lb
L	section normal force, lb/ft
M	local Mach number
M_c	section aerodynamic moment about local quarter chord, in lb/ft
M^2C_L	nondimensional section normal force, $\dfrac{2L}{a^2\rho c}$
M^2C_M	nondimensional section pitching moment, $\dfrac{2M_c}{a^2\rho c^2}$
M^2C_{pa}	nondimensional upper surface pressure, $\dfrac{2(p-p_\infty)}{a^2\rho}$
n_z	load factor, g
p	surface pressure, lb/in^2
p	static pressure, lb/in^2
q	dynamic pressure, lb/in^2
r	radial location, ft
R	blade radius, ft
x	chord location, in
ρ	air density, slug/ft^3
σ	rotor solidity, $\dfrac{bc}{\pi R}$
Ω	main rotor speed, rad/sec

1.0 INTRODUCTION

Knowing the airloads distribution on a rotor blade in flight is fundamental to understanding how a rotor works and for designing new and improved rotorcraft. Obtaining the airloads, however, is a difficult measurement task since many pressure transducers must be installed on the blade to adequately capture the airloads behavior. In addition, acquiring and processing the resulting unsteady pressure data is nontrivial. Hooper[1] in his 1983 survey, identified ten programmes where pressure measurements were obtained for at least five radial stations on a rotor in either a flight or a windtunnel test. Eight of these data sets[2–12] were obtained on conventional helicopters and two[13, 14] were obtained for compound aircraft. The data obtained, particularly Refs 4, 5, 9, and 12, have been very valuable in obtaining a general understanding of the complex air flow over a helicopter blade in flight and for supporting development of analyses. Despite the usefulness of these data, however, a data set with increased bandwidth and a greater range of flight conditions than previously obtained was needed.

The present flight test program[15–17] was designed to overcome weaknesses of past programs in terms of the quality and quantity of data, the bandwidth of the data, and ease of accessibility to the data. The flight test portion of the program is now complete and some data is now being used to validate comprehensive analyses[18, 19]. The purpose of this paper is to provide an overview of the flight program content and some representative accomplishments. The paper begins with a brief discussion of the flight program background. The rotor

Paper No. 2231. Manuscript received 13 December 1996, accepted 3 April 1997
Paper first presented at the 22nd European Rotorcraft Forum, September 1996, Brighton, UK. Organised by the Royal Aeronautical Society.

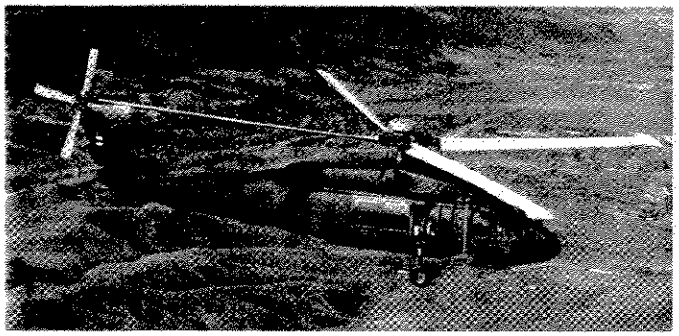

Figure 1. UH-60A with instrumented blades.

and aircraft instrumentation are described, followed by a description of the on-board data acquisition system, which was the biggest technical challenge of the program. Finally, a limited set of airloads data from two flight conditions are shown.

2.0 PROGRAM BACKGROUND

The flight test of the pressure-instrumented UH-60A rotor is one aspect of a larger program to obtain comprehensive measurements on a current technology rotor. In addition to flight testing, the program includes small and full-scale windtunnel testing. The small-scale testing was completed using a 1:5·73 scaled UH-60A model rotor in hover[20] and forward flight[21]. Full-scale windtunnel testing is planned for the National Full-Scale Aerodynamic Complex (NFAC) at Nasa Ames Research Center following installation and checkout of a new rotor test stand, the Large Rotor Test Apparatus (LRTA).

The UH-60A flight testing was conducted in two phases. The first phase was conducted in a cooperative program with the US Army Aviation Engineering Flight Activity at Edwards AFB to establish some of the flight test procedures to be used during the second phase using the highly-instrumented rotor. These tests, completed in June 1987, used a blade (with limited structural instrumentation) made for the US Air Force's HH-60D Night Hawk program. The Phase 1 tests totaled 57 flight hours[22, 23].

The second phase of the UH-60A flight test program, with the highly-instrumented blades installed, was intended to cover an extensive range of test conditions in a number of separate test campaigns. Testing, however, was delayed because of difficulties that were encountered in the development of the data acquisition system. A successful system was finally demonstrated yet, the test program was subsequently reduced in scope to a single test campaign. A restricted program was defined that included

1. level flight
2. manoeuvres
3. ground-measured acoustics
4. airborne-measured acoustics
5. flight dynamics.

This reduced program was started in July 1993 and was completed in February 1994. The UH-60A Airloads aircraft, shown in Fig. 1, made 31 data flights during this time period for a total of 57 flight hours[24].

3.0 INSTRUMENTATION

A total of 362 parameters (Table 1) were measured on the instrumented rotor blades and hub, and another 93 parameters (Table 2) were measured on the aircraft. This section provides brief descriptions of the various sets of instrumentation. Special procedures were used to calibrate some of the instrumentation suites and, as appropriate, those calibrations are discussed here.

Measurement group	Number of sensors	Sample rate, per second	Filter frequency, Hz
Blade pressures	242	2142	550
Blade temperature	50	357	—
Blade flap, edge, and torsional moments	21	357	110
Blade feather, flap, and lag angles	12	357	110
Blade pitch link and damper load	8	357	110
Blade flap and edge acceleration	20	357	110
Shaft bending and torque	2	357	110
Hub and bifilar mass acceleration	7	357	110

Table 1
Blade and hub rotating measurements

3.1 Blade pressures

The pressure blade was built with 242 sub-miniature, pipette-type absolute pressure transducers[25] embedded below the skin surface of the blade. In order to maintain instrumentation integrity, the blade design specifications required that all sensors be replaceable, and that each chordwise array have spare wiring. This was accomplished with the exception of the pressure transducers inside the removable tip cap which are not individually replaceable. Instead, a second fully-instrumented tip cap was made and then kept as a spare. The pipettes of the pressure transducers have an outside diameter of 0·1 mm and are mounted flush with the aerofoil sections with minimal effect on the aerodynamic flow. Blade contour measurements at each radial array verified that the aerofoil contour was not changed. The main spar of the blade was not modified during installation of the transducers, thus maintaining blade structural integrity and blade dynamics. The instrumented blade dynamic characteristics were measured by Hamade and Kufeld[26]. Each pressure transducer was statically calibrated over a range of 2 to 18 psia and its frequency response measured to 10 000 Hz. Most of the transducers show a flat response to 2000 Hz. The effects of temperature, centrifugal force and vibratory loading on the pressure transducers were measured[25].

Table 2
Aircraft measurements

Measurement group	Number of sensors	Sample rate, per second	Filter frequency, Hz
Aircraft states and controls	42	209	36
Engine states	13	209	36
Cabin vibration accelerometers	32	418	108
Control loads/ tail rotor torque	6	836	108

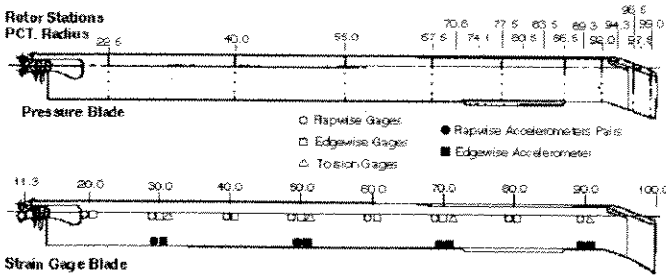

Figure 2. Schematic of pressure transducer, strain gauge and accelerometer locations along UH-60A rotor blades.

The layout of the transducers is shown in Fig. 2. The spacing of the transducers was selected to allow for accurate, integrated measurements of chordwise and spanwise loads and to capture the most important aerodynamic phenomena on the blade.

A pressure calibration technique was developed for rapid calibration of the pressure transducers once they were installed in the blade. A mylar sleeve was placed over the blade and both ends were sealed with a flexible sealing compound. Near the root, the tube was sealed against the aerofoil section of the blade; near the tip, the sleeve was sealed against itself forming an airtight chamber. Between the blade and sleeve was a breather cloth to allow the free flow of air along the length of the blade and to prevent the mylar from sealing off any of the pressure transducers. A vacuum pump and control unit was then attached to the sleeve and air was removed from the sealed sleeve to create a uniform pressure field around the blade down to 8 psi, (the tip cap structural limit). Data were collected through the Rotating Data Acquisition System (RDAS), the same system that was used in flight, to determine calibration slope and offset for each of the 242 pressure transducers at one time. The calculated gain values were stored in a Cal File for the next series of flights. This calibration was repeated about every two to three weeks during the test program.

3.2 Blade temperatures

Fifty pressure transducers were designed to independently measure blade temperature in addition to pressure. These transducers were distributed in five radial arrays on both the top and bottom of the blade at 0·22R, 0·44R, 0·675R, 0·865R, and 0·965R. The temperature transducers were calibrated as installed in the blade for the range of −5°C to 58°C. These temperature measurements provide the capability to correct the blade pressure for thermal effects, although this is not currently done.

3.3 Strain gages and accelerometers

Strain guages and accelerometers were installed in the second instrumented blade during the fabrication process. Blade flap, chord, and torsional moments were measured with a total of 21 two- or four-leg strain gauge bridges bonded directly to the spar of the blade. The measurements were evenly distributed along the blade radius as shown in Fig. 2. The blade was calibrated statically with an applied load. Corrections for the blade twist distribution were made in the applied loading, but guage cross-coupling effects were assumed small and left uncorrected.

A total of twelve accelerometers were bonded to the leading and trailing edges of the spar of the strain gauge blade and were completely enclosed within the contour of the aerofoil section. Eight of the twelve accelerometers measured flapwise accelerations and four measured edgewise accelerations. They were placed at four evenly spaced radial stations as shown in Fig. 2. The flapwise accelerometers were installed as pairs fore and aft of the spar which allows the calculation of torsional as well as flapwise acceleration. The accelerometers were calibrated prior to installation.

Additional blade accelerometers were mounted atop each blade clevis at 0·088R and 0·125R to allow estimation of blade flapping[27]. In addition, an accelerometer was added to each bifilar mass to measure in-plane absorber acceleration. A triaxial set of accelerometers was mounted inside the RDAS near the center of rotation to measure hub vibration. A survey of the hub vibration results is reported by Studebaker[28]. Each of these fifteen accelerometers was readily removable for laboratory calibration.

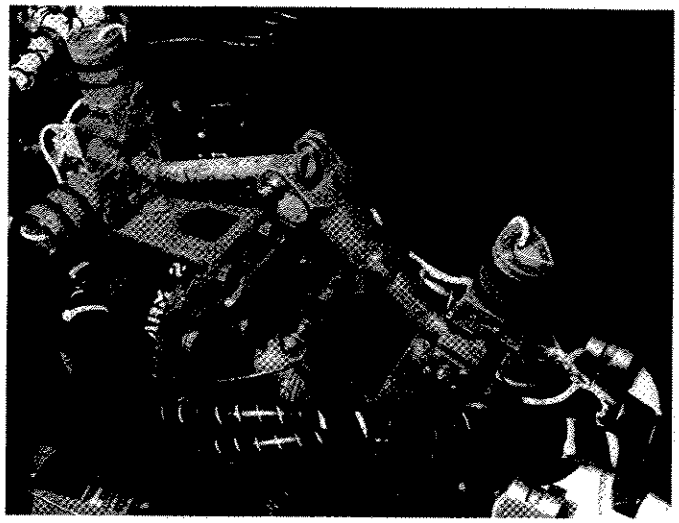

Figure 3. UH-60A blade motion hardware.

The four pitch links and dampers were instrumented with four-leg, strain gauge bridges that measured axial force on the pitch links and dampers. The main rotor shaft extension was instrumented with two four-leg strain gauge bridges to measure shaft bending and torque. The shaft extension was calibrated at Sikorsky Aircraft's calibration laboratory prior to the flight test program. Calibrations and measurements of hub moments were not made during this test program.

3.4 Blade motion hardware

The UH-60A has a fully-articulated main rotor system which incorporates an elastomeric bearing to allow independent blade flap, lag and feather motion. Because of this elastomeric bearing configuration, direct measurement of blade motion with rotary potentiometers or similar devices was not possible. Instead, a specially designed blade motion measurement device known as the Blade Motion Hardware (BMH) was used to obtain blade flap, lag and feather measurements on each blade.

The BMH (Fig. 3) uses three, rotary variable differential transformers (RVDTs) to measure rotations which approximate blade flap, lag and feather motions. Since the BMH was not located at the blade hinge point, the RVDT measured coupled blade motions. The true blade motions were obtained through three kinematic equations which account for the blade coupling. The kinematic equations for each blade include ten coefficients that were determined by calibration.

3.5 Aircraft state measurements

The aircraft state measurements included airspeeds; angular attitudes, rates, and accelerations; linear accelerations; and angle of attack and sideslip from vanes mounted on the test boom. The airspeed measurements were obtained using three independent systems: the test boom, the manufacturer-installed aircraft system, and a low-speed system called the Helicopter Air Data System (Hads). The boom and aircraft measurements were used for airspeeds above approximately 30 knots. The Hads was used to obtain airspeed data below 30 knots.

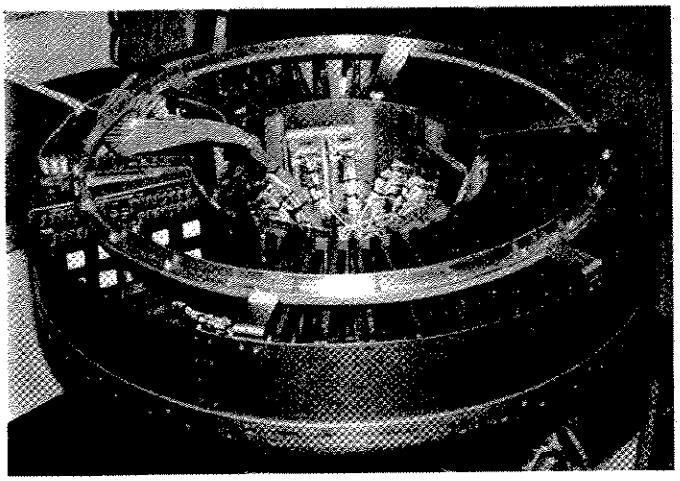

Figure 4. View of signal conditioning cards and encoders inside the RDAS.

3.6 Fuselage vibration

There were 35 fuselage accelerometers mounted in the aircraft measuring lateral, longitudinal, and vertical accelerations. Vibration was measured in the cockpit and cabin, and on the transmission, cabin absorber, tail, and stabilator. The sensor locations match those of a ground vibration test conducted on a different UH-60A vehicle configured similarly to the Airloads Program's aircraft[29].

3.7 Flight controls

The flight control positions were measured using conventional displacement transducers such as potentiometers and linear variable differential transformers (LVDTs). In addition to the pilot control positions, the control mixer inputs, the Stability Augmentation System (SAS) actuator positions, and the flight control servo positions were also measured. Control position calibration was standard except for the SAS actuators which were calibrated by inputting a hardover signal into the flight control computer with a signal generator box provided by Sikorsky Aircraft.

3.8 Engine states

Engine state measurements were obtained from standard instrumentation provided by the engine manufacturer except for the fuel flow measurements. The fuel flow measurements were provided by separate turbine-type meters installed in the fuel lines.

4.0 DATA ACQUISITION

Flight data from the UH-60A Airloads aircraft were obtained with two airborne data acquisition systems. The first system, the Rotating Data Acquisition System (RDAS), was mounted atop the rotor hub and collected data from main rotor sensors. The second system, the Airframe Data Acquisition System (ADAS) was mounted inside the cabin and collected data from non-rotating components plus RDAS and ADAS health monitoring information. The main RDAS and ADAS measurement groups are summarized in Tables 1 and 2, respectively, including, the sample rates and filter frequencies. For a limited number of test conditions, ground-based tracking data were also obtained and merged with the aircraft data.

4.1 Rotating data acquisition system (RDAS)

The RDAS was developed and built at Ames Research Center and represents a major step forward in "state-of-the-art" flight data acquisition hardware. The operation of this system in a helicopter flight environment was one of the biggest risks undertaken by this program. The high reliability of the RDAS throughout the flight program was a key element in the program's success.

The RDAS was designed around ten identical Pulse Code Modulation (PCM) encoders and has a system data bit rate of 7·5 megabits per second. The ten encoders were mounted in the centre of a hub mounted container surrounded by over 40 integrated circuit cards in a hub and spoke configuration (see Fig. 4). Data sampling was controlled by a common synchronisation pulse sent to all ten encoders from a timing integrated circuit card inside the RDAS. Each encoder was programmed in an identical manner collecting 35 ten-bit, mainframe words, which include time code, rotor position and run counter data to ensure data synchronisation. The ten-bit encoders provide a useful range of 1000 counts for analogue inputs and 1024 counts for bi-level (digital) inputs. The maximum encoder bit rate of 750 kilobits per second provides 2142·6 samples per second for each main frame parameter. Five of the main frame words were set up in a six-deep, sub-commutation configuration providing a lower sample rate of 357·14 samples per second for 180 sensors, which included blade temperatures, blade loads, pitch link and damper loads, blade accelerations and motions.

Forty of the integrated circuit cards were identical signal conditioning cards which provided space for filters and gain amplifiers for 320 transducers. The gain and offset of each transducer (with the exception of temperature measurements) were controlled by high precision resistors that were soldered to the signal conditioning cards. Each resistor was specifically selected to obtain the optimal match with that channel's transducer output. This enabled the 10-bit RDAS system to deliver an average resolution of 0·026 psi per count for the pressure transducers. This method of gain and offset control provided a low sensitivity to temperature variation and withstood the high dynamic loads of the rotating hub in flight.

All data from transducers mounted on the blades, pitch links, dampers, and the rotor hub were passed through either 550 or 110 Hz six-pole, Butterworth filters and gain amplifiers to sample-and-hold amplifiers. The signals were then digitized by the ten encoders and were stored as a digital stream. The ten digital data streams were then sent down through a slip ring into the aircraft cabin.

Inside the cabin, the ten streams were inspected for valid encoder signals and were then combined by a multiplexer into a single 7·5 megabit per second stream for rapid post flight processing using one ground based computer. Before multiplexing, data from any one of the ten streams could be sent to the ground station for real time monitoring. The multiplexed signal was then routed through a digital spreader unit which divided the data stream into nine tracks, each with an alignment tag, which were then recorded onto a 14 track Frequency Modulation (FM) tape recorder. This step was necessary as FM tape recorder technology cannot reliably handle the single-stream rate. During post-flight data processing the nine data streams were re-merged with the help of the alignment tags into a single stream again for processing.

4.2 Airframe data acquisition system (ADAS)

The ADAS acquired data from all non-rotating measurements, including aircraft and engine states, control positions, and system health monitoring parameters. In contrast to the ten-bit PCM encoders used in the RDAS, the ADAS incorporated 12-bit PCM encoders. The 12-bit encoders provided a useful range of 4000 counts for analogue inputs and 4096 counts for bi-level (digital) inputs. The system dynamic range was approximately 72 dB.

The ADAS featured adjustable system gain to allow compatibility with a variety of sensor output voltage levels. The PCM encoder gain was variable from 0·5 to 20, while the gain of the signal conditioning modules was limited to 1, 8 and 250. Unlike the RDAS, these gains were programmable and did not require resistor changes.

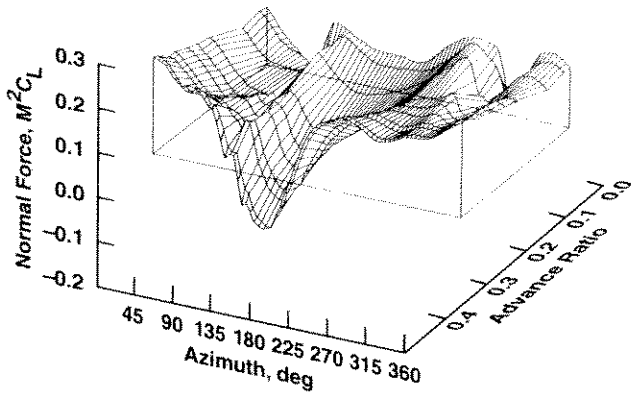

Figure 5. Section normal force as a function of blade azimuth and advance ratio; $C_w/\sigma = 0{\cdot}08$, $r/R = 0{\cdot}92$, 0 to 60 harmonics.

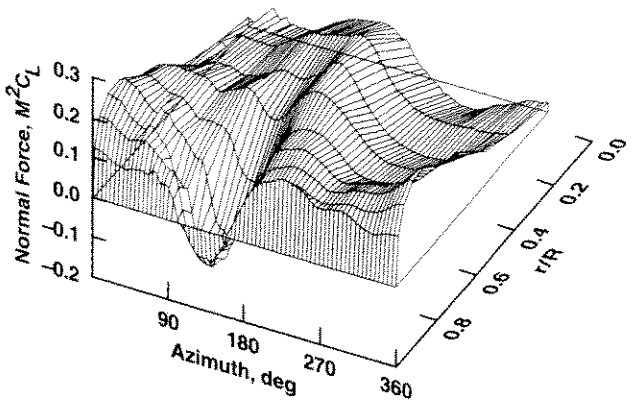

Figure 6. Section normal force as a function of blade azimuth and radial station (Counter 8534); $C_w/\sigma = 0{\cdot}08$, advance ratio = 0·368, 0 to 60 harmonics.

The product of the encoder gain and the signal conditioning gain yielded the effective system gain for a particular measurement.

As installed in the UH-60A Airloads aircraft, the ADAS had three available anti-aliasing filter modules. These three filters had –3 dB points at approximately 36, 72 and 108 Hz. The PCM bit map was designed to provide a minimum sample rate of four times the filter cutoff frequency. The nominal sample rates for the low- mid-, and high-rate parameters were: 209, 418, and 836 samples per second. As configured for this test, the ADAS could acquire data up to 115 individual measurements.

5.0 TEST ENVELOPE

Flight test data were obtained for over 900 test conditions. As discussed previously, these test conditions can be roughly categorised as

1. level flight
2. manoeuvres[30]
3. ground-measured acoustics[31]
4. flight-measured acoustic
5. flight dynamics.

The helicopter was flown within the limits establish by the US Army Operator Manual[32]. The helicopter was able to reach maximum allowable airspeed of 193 knots, load factors up to 2g and as low as 0·25g and an altitude of 18 000 ft. The structural limits of the helicopter were not the major limiting factor for testing because the aircraft would reach the engine limits first.

6.0 AIRLOADS MEASUREMENTS

This section will provide sample results for two test conditions from the first two categories. The test conditions were selected because they represent two levels of complexity for the analyst: a steady-state, unaccelerated flight condition and a steady manoeuvre with constant angular rates.

6.1 Level Flight

Steady, level-flight airspeed sweeps were flown for six values of C_w/σ to provide baseline airloads data that show the effects of advance ratio and blade loading[33]. The limiting condition in each level flight sweep was the 30 minute engine power limit. Figure 5 shows the evolution of the airloads with advance ratio at $0{\cdot}92R$, the radial location just inboard of where the blade sweep starts. This surface plot shows the nondimensional section normal force as a function of blade azimuth and advance ratio. Advance ratio varies from 0·093 to 0·368 and each advance ratio line on the surface plot represents a separate test condition. At low speeds the influence of vorticity loading from the tip vorticies of previous blades is clearly evident on the advancing side of the disk where there is a down-up pulse and on the retreating side where there is an up-down pulse. This vorticity loading peaks at an advance ratio of about 0·1 and is the source of the high vibratory loading that is observed in transition flight. As advance ratio increases the loading caused by the tip vortices diminishes, but the influence is still visible on this plot beyond an advance ratio of 0·3. The character of the section normal force changes as advance ratio increases so that the normal force is reduced in the second quadrant to maintain roll moment balance on the aircraft[1]. At this radial station the normal force is negative for advance ratios beyond 0·20. The basic loading shown here appears typical for rotors in forward flight[34].

The blade airloads at the highest speed condition in Fig. 5 are shown in Fig. 6 as a function of blade azimuth and radial station. Each line on the surface plot represents the normal force at a particular radial station from the most inboard station at $0{\cdot}225R$ to the most outboard at $0{\cdot}9R$. The section normal force at $1{\cdot}00R$ is zero. At the most inboard station on the rotor the normal force is largest over the nose of the aircraft and then decreases rapidly and becomes negative in the third and fourth quadrants because of reverse flow. Moving out on the blade the normal force is positive in all quadrants and tends to concentrate over the fore and aft portions of the rotor disk. A section of reduced loading develops in the second quadrant because of the need to maintain roll-moment balance and the normal force first reaches zero at $0{\cdot}775R$ for this airspeed. The region of negative normal force in the second quadrant is greatest at $0{\cdot}92R$ and becomes less negative as the blade tip is approached. This behavior is very similar to the normal force distributions examined by Hooper in his study[1].

The data shown in Figs 5 and 6 are from the first revolution of the test condition. Approximately five sec of data were obtained for each condition; the full record contains approximately 19 or 20 revolutions (or cycles) of data. Coleman and Bousman[33] demonstrated the steadiness of these data for level flight cases by showing the time histories of a pressure transducer on the lower surface as a shock passes over the transducer for the high-speed test condition of Fig. 6. Figure 7 shows a similar plot for a pressure transducer on the upper surface near the leading edge. In this figure the nondimensional pressure is shown as a function of blade azimuth and cycle count. Steadiness in the data is shown by the smoothness of the plot surface. For the case shown here, two different phenomena are seen. First, just at the start of the second quadrant, a small variation in pressure is observed. Tung and Bousman[35] suggest this variation is caused by a pair of vortices; one vortex shed from the region of positive loading on the previous blade and the other vortex, of opposite sign, shed from the region of negative loading. The loading from this vortex pair is seen to be steady and repeatable. Second, a much stronger

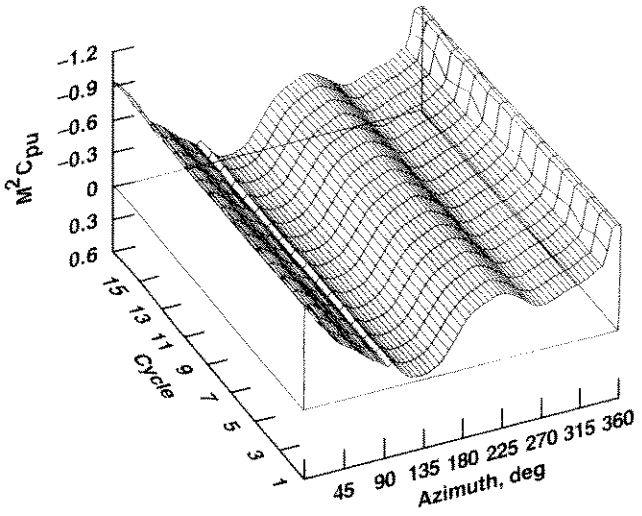

Figure 7. Upper surface pressure as a function of blade azimuth and cycle number (Counter 8534); $x/c = 0{\cdot}030$, $r/R = 0{\cdot}865$, $C_w/\sigma = 0{\cdot}08$, advance ratio = 0·368, 0 to 60 harmonics.

change in pressure is evident at the end of the fourth quadrant where a shock passes over the transducer location. The shock is quite strong during this initial passage as the angle of attack is quite high over the aft portion of the disk. As the blade enters the first quadrant the angle of attack is decreasing very rapidly and the area of supercritical flow is reduced such that a returning shock does not occur at this location. Despite the rapid variation in angle of attack around the rotor disk and the resulting strong pressure gradients, Fig. 7 shows that the data are very steady over the entire length of the record. Only a slight unsteadiness is seen during the pressure rise associated with the shock passage.

In some cases, the airloads are noticeably unsteady over the five-second period of a test condition. For the highest loading condition, $C_w/\sigma = 0{\cdot}13$, the rotor undergoes two dynamic stall cycles[33] at the power limiting advance ratio of = 0·236. During these stall cycles, there is considerable unsteadiness in the airloads as well as elastic motion in the rotor. Fig. 8 shows the nondimensional section moment at $0{\cdot}865R$ for this case as a function of blade azimuth and cycle count. The section pitching moment is relatively stable in the first three quadrants of the rotor, but then considerable unsteadiness is observed over the two dynamic stall cycles starting just prior to 270° and finishing near the beginning of the first quadrant. The average

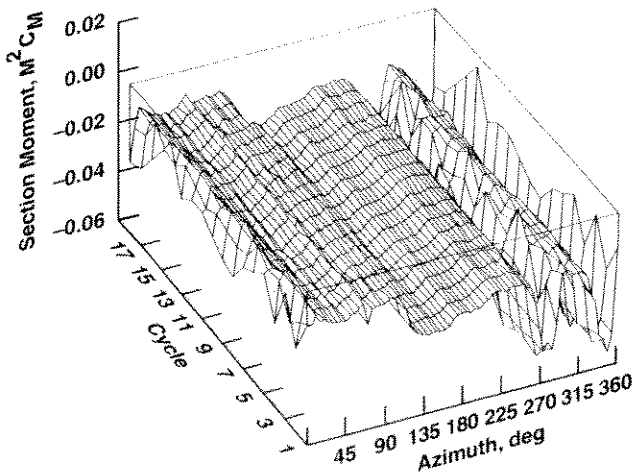

Figure 8. Section pitching moment as a function of blade azimuth and cycle number (Counter 9017); $r/R = 0{\cdot}865$, $C_w/\sigma = 0{\cdot}13$, advance ratio = 0·236, 0 to 60 harmonics.

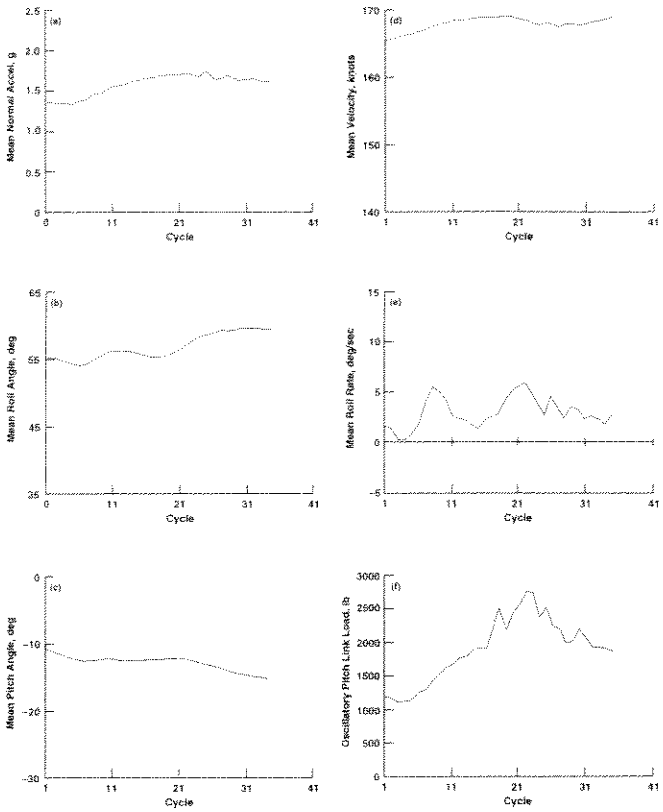

Figure 9. UH-60A (a) mean load factor, (b) mean roll attitude, (c) mean pitch attitude, (d) mean airspeed, (e) mean roll rate, and (f) mean pitch-link load for each rotor cycle of an high speed steady right turn (Counter 11 679).

loading in this case represents a good test of dynamic stall models; also, the measured unsteadiness is important for understanding and modeling of dynamic stall mechanisms.

6.2 Diving turn

The diving turn data shown here are from a steady manoeuvre with a target right bank angle of 55° and an airspeed of 140 KIAS (Counter 11679). The aircraft descended at approximately 3500 feet per minute to obtain this airspeed and bank angle (load factor). Although the manoeuvre is described as a steady turn, the pilot had difficulty maintaining a true steady condition for the entire 10 second record. Figure 9 shows several of the aircraft state measurements to indicate the steadiness of the manoeuvre. Although the target airspeed and bank angles were achieved near the beginning of the manoeuvre, the load factor was still increasing from 1·3g to the maximum value of 1·7g obtained midway through the manoeuvre. The oscillatory pitch-link loads show similar behavior, increasing from 1100 lb to 2700 lb, and were clearly sensitive to the rotor load factor. Near the middle of the record when the pitch link loads were greatest, the pilot was able to hold conditions relatively steady for several rotor revolutions. Figure 10 provides a more detailed look at the pitch link load variation for this section of the manoeuvre (cycle 11 to 26) in an offset plot format to quantitatively assess the effect of aircraft steadiness on the pitch-link loads.

The variation in the pitch-link loads during the manoeuvre occurs primarily in two location, at 70° and 270° blade azimuth. At both locations, the load varies significantly from one cycle of the manoeuvre to the next. However, there is one section of four consecutive cycles (20 to 23) with very little variation in the pitch link load. This test condition provides sufficiently steady data to allow correlation with analysis. The revolution selected for review in this paper will

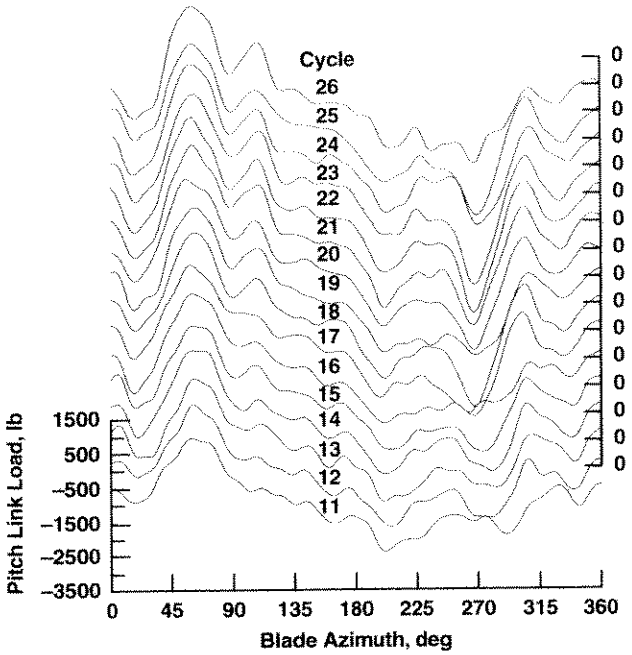

Figure 10. Offset plot of pitch-link load as a function of azimuth and rotor revolution during high speed steady turn (Counter 11 679); 0 to 24 harmonics.

be the 22nd revolution, which is centered in the steadiest portion of the manoeuvre.

The non-dimensional blade section normal force for cycle 22 is shown in Fig. 11. Compared to the steady level flight condition of Fig. 6, both similarities and differences are seen. The areas of negative force at the tip in the second quadrant and at the blade root in the third and fourth quadrants are similar to those seen in the level flight case. Because of the increased thrust on the rotor, however, the section normal force is substantially increased and more higher harmonic content is seen in the airloads. One major difference is found near the blade tip, where a very large, but narrow region (about 15°) of normal force is observed around 55° rotor azimuth. This short-term spike in the blade lift, which is seen as far inboard as r/R = 0·675, is a nonlinear aerodynamic event due in part to the rapidly increasing Mach number on the advancing blade, the decreasing pitch angle of the blade needed to balance the roll moment of the rotor in forward flight, and blade flexibility. Immediately following the normal force spike in the first quadrant, negative loading results as the blade pitch continues to decrease in the second quadrant. The normal force becomes positive again as the rotor blade

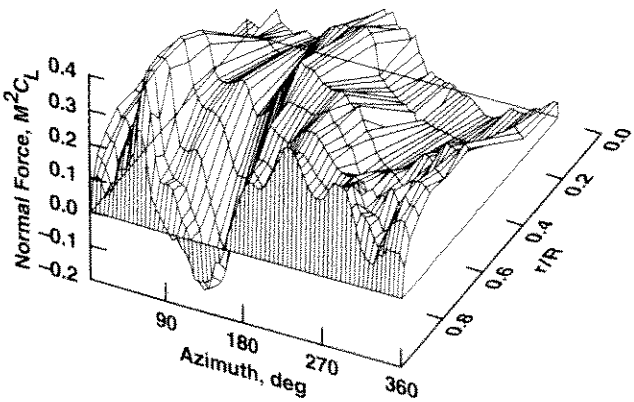

Figure 11. Section normal force as a function of azimuth and radial station during a high-speed, steady right turn (Cycle 22, Counter 11 679); 0 to 60 harmonics.

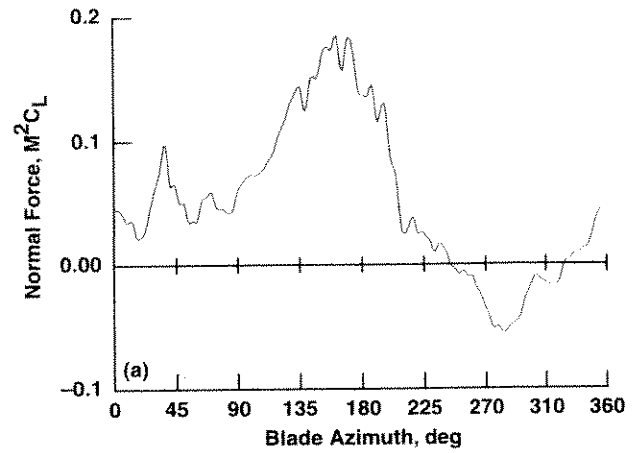

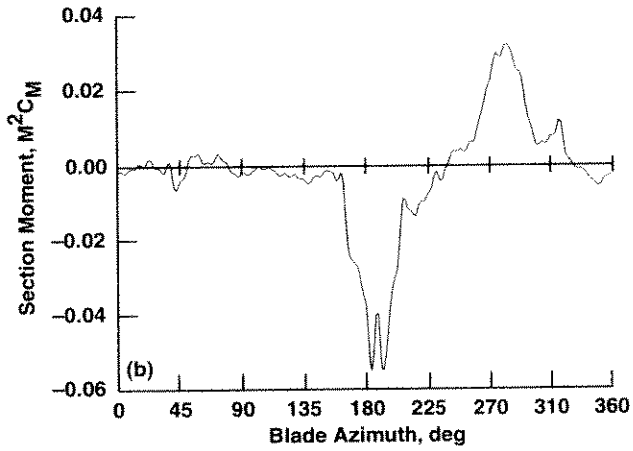

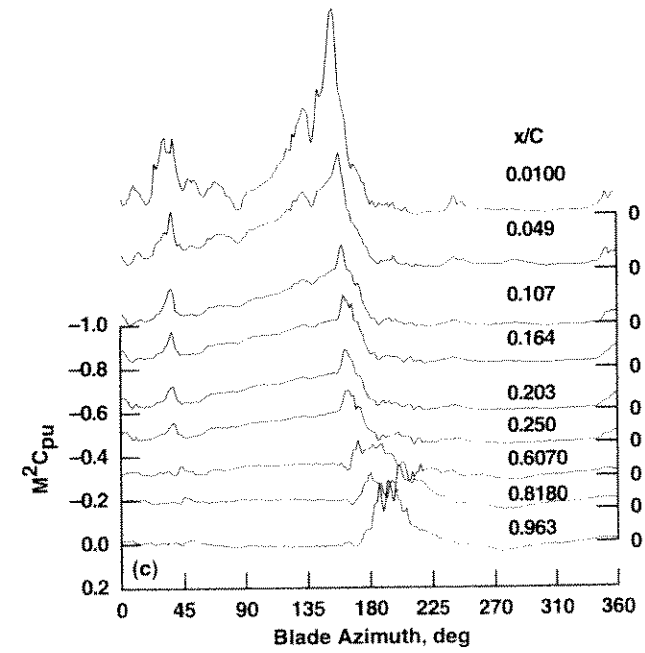

Figure 12. (a) Section normal force, (b) section moment, and (c) an offset plot of upper surface pressures *vs* rotor azimuth for r/R = 0·225, (Cycle 22, Counter 11 679); 0 to 60 harmonics.

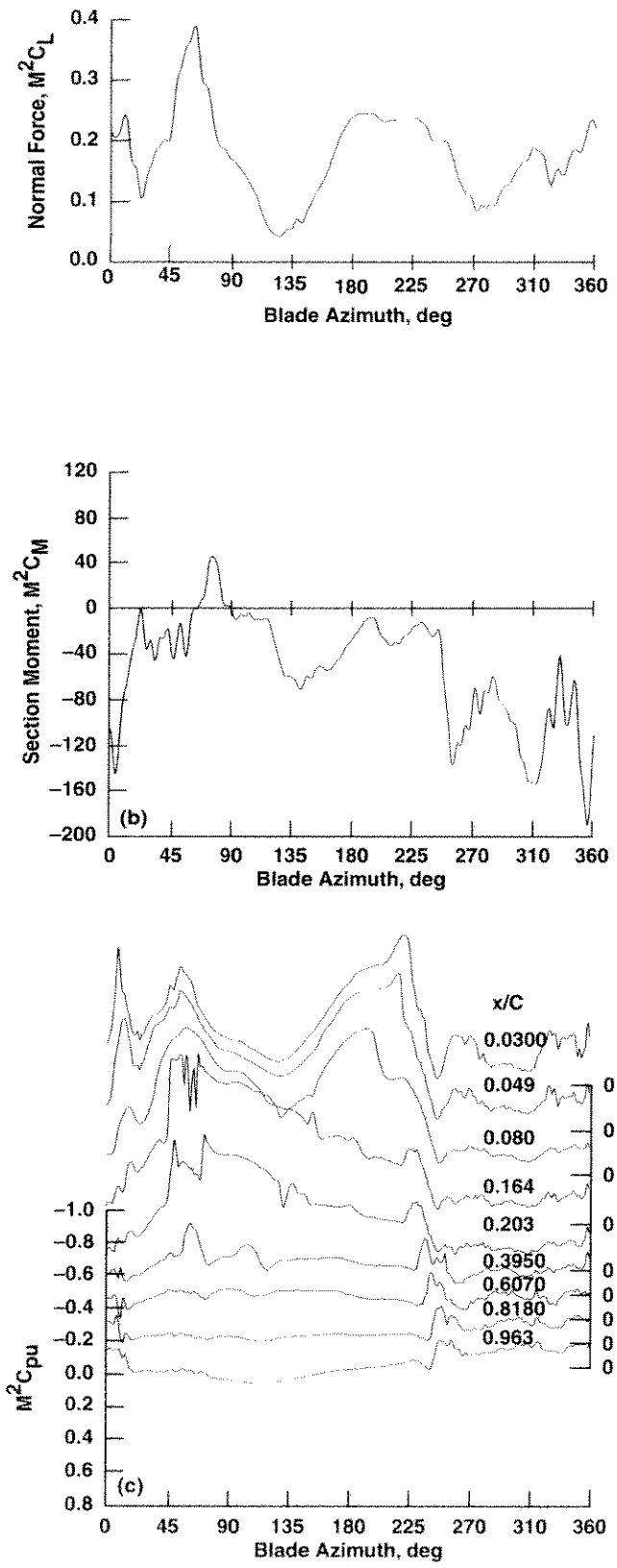

Figure 13. (a) Section normal force, (b) section moment, and (c) an offset plot of upper surface pressures *vs* rotor azimuth for $r/R = 0{\cdot}775$, (Cycle 22, Counter 11 679); 0 to 60 harmonics.

enters the third quadrant and is maintained into the fourth quadrant where, near 315° rotor azimuth, a rapid drop in normal force is seen. Oscillations in normal force then occur as the blade encounters a number of dynamic stall cycles that extend into the first quadrant.

A closer examination of these airloads is provided in Figs 12–14 for the $0{\cdot}225R$, $0{\cdot}775R$, and $0{\cdot}92R$ stations.

In Fig. 12 the section normal force, moment and upper surface pressures are shown for $r/R = 0{\cdot}225$. The section normal force in the first quadrant is low or moderate with a pulse-like force increment around 35°. The normal force increases substantially in the second quadrant and reaches a maximum just before 160°. The normal force then rapidly decreases, becoming negative in the third and fourth quadrants in the region of reversed flow. The section moment (Fig. 12(b)) is quite low on the advancing side of the disk, but near 170° the moment rapidly becomes negative — an indication of blade stall. The upper surface pressure (Fig 12(c)) clearly shows a convective event associated with a dynamic stall vortex formed at the leading edge at about 150° and then moving along the aerofoil surface and leaving the trailing edge at about 200°. The minimum moment that is encountered coincides with the departure of the dynamic stall vortex from the trailing edge. The angle of attack is relatively high prior to the shedding of the dynamic stall vortex and the flow in the immediate vicinity of $0{\cdot}010c$ is supercritical at this azimuth. The region of supercritical flow is quite limited, however, and does not extend back to the next transducer at $0{\cdot}049c$. Although no measurements were made of the fuselage induced flow, in this case, the upwash over the aircraft nose probably increases the local angle of attack and affects the stall characteristics[36].

The section moment, in Fig. 12(b), shows a positive moment in the third and fourth quadrants that is nearly as large as the negative moment induced by dynamic stall. For the most part, this positive moment is a result of the negative normal force on the aerofoil in the reverse flow region with the centre of pressure near the aerofoil three-quarter chord. Interestingly enough, the lower surface pressures (not shown here) indicate that a dynamic stall vortex is shed from the trailing edge moving towards the leading edge on the lower surface in the reverse flow region.

Additional aerodynamic events indicated in Fig. 12 include a blade-vortex interaction at about 35° which causes the impulse-like normal force in the first quadrant and possibly a second blade-vortex interaction at about 130°. Little moment change is seen during those blade-vortex interactions.

The airloads measured in the diving turn at $0{\cdot}775R$ are shown in Fig. 13 and the loading is more complex than seen inboard. This complexity results primarily from the extensive regions of supercritical flow, but also from substantial torsional deformation outboard on the blade. The nondimensional section normal force (Fig. 13(a)) shows a large increment in the first quadrant; as discussed previously, this force increment or spike extends for only 15 or 20°. The normal force is reduced in the second quadrant, increases in the third quadrant, and then drops to a moderate level in the fourth quadrant. The section moment shows a number of oscillations, with a maximum negative spike at 245°.

The airloads behavior at $0{\cdot}775R$ is best understood by a re-examining of the pitch-link loads in Fig. 10. Although these loads are the axial force in the pitch link, they also correspond to the torsional moment at the blade root. As a first approximation these loads are qualitatively representation of the blade's elastic deformation. Thus, following the rapid negative pitching moment at 245° (Fig. 13(b)), the blade twists down, reducing the angle of attack, and then twists up again, showing a peak deformation near 300° as seen in Fig. 10. Three subsequent cycles are also apparent in Fig. 10 with maxima at 5°, 60° and 105°. The pulse-like normal force increment in the first quadrant (Fig. 13(a)) is a combined effect of increasing angle of attack from 30–60° (Fig. 10) and increasing Mach number. Supercritical flow develops on the first 20–40% of the aerofoil at about 45° (Fig. 13(c)) and this greatly increases the section normal force. As the blade starts to twist down again the normal force is reduced but the upper surface pressures do not indicate a convective event as-

sociated with dynamic stall. The blade twists up again toward 105°, but the root pitch angle is rapidly decreasing so the combined effect is an inflection point in the normal force around 90°. Relatively small oscillations in section moment are observed in the first and second quadrants but these are probably caused by relative upper and lower surface shock motion as described for a high-speed dive case by Kufeld and Bousman[37].

The normal force recovers in the third quadrant as the root pitch angle increases and the elastic twist reduces to smaller values. The flow is supercritical over the first 10% of the aerofoil in this quadrant and, as shown in Fig. 13(c), there is a rapid decrease in the upper surface pressure at about 220° as an apparent dynamic stall vortex forms and is shed near 0·049c. Although the suction peak at 0·030c is maintained for another 5° or so after the collapse of the peak at 0·049c. This event is convective and moves back along the surface of the of the aerofoil and leaves the trailing edge at about 250°. The passage of the dynamic stall vortex coincides with the negative pitching moment peak.

Following the first dynamic stall oscillation that starts at 220°, the section moment (Fig. 13(b)) shows a number of oscillations in the fourth and first quadrants which tend to be out-of-phase with the torsion moment (see Fig. 10). The flow appears to remains separated at the trailing edge until about 20° (Fig. 13(c)), as shown by the drop in pressure at the trailing edge transducer, and there is only weak evidence in the surface pressures of additional dynamic stall cycles.

The airloads at 0·92R are examined in Fig. 14. The section normal force distribution is similar to the that at 0·775R, but the section moment shows a number of differences including additional high loading oscillations on the advancing side of the disk. The pulse-like normal force increment is again seen in the first quadrant and, as was discussed for the 0·775R section, is a combined effect of the rapid increase in angle of attack caused by elastic twist and increasing Mach number creating a large area of supercritical flow over the front of the aerofoil. Unlike the inboard case, however, a dynamic stall vortex is apparently shed. Fig. 14(c) shows that a dynamic stall vortex is shed in the first 10% of the aerofoil around 55° azimuth. The vortex creates a region (from 0·107 to 0·250c) of subcritical flow within the area of supercritical flow on the aerofoil. By 0·395c the vortex passage is clearly seen as a convective event and it leaves the trailing edge of the aerofoil by approximately 65°. Other dynamic stall cycles are seen from 285°–295° and 355°–5° and, in fact, these are the initiating stall cycles in the sequence of torsional oscillations. Note that the initiating point of the first dynamic stall cycle at 285° (Fig 14(c)) is delayed compared to the initiating point observed in Fig. 13 at 220°.

The negative section moment peaks in Fig. 14 at 60°, 285° and 355° appear to be associated with the passage of dynamic stall vortices off the trailing edge of the aerofoil. The negative moment peaks at 110° and 145° are not associated with any dynamic stall events. Rather, these large negative moments are associated with rapid and unequal motion of the supercritical flow regions on the upper and lower surfaces of the aerofoil. The combined effect of angle of attack and Mach number influence the extent of the supercritical flow regions. Azimuths where these flow regions are unbalanced result in momentary large pitching moments (this was shown for a similar high-speed dive case in Ref. 37).

The airloads shown in Figs. 12–14 and, particularly, the dynamic stall characteristics, are similar to the behavior shown in Ref. 28 for the UTTAS manoeuvre. These similarities include the general form of the pitch-link motion with three of four cycles of oscillation; the inception of the first dynamic stall vortex inboard on the aerofoil at 0·775 or 0·865R with the resulting azimuthal delay in vortex shedding towards the tip of the blade; and the interaction observed in the first quadrant between the shed dynamic stall vortex and the upper surface supercritical flow. Differences in the airloads behavior are also seen; these include the absence of repeated dynamic stall vortex shedding at 0·775 for the present diving turn and the large pitching moments outboard that are caused by out-of-phase shock motion on the upper and lower surfaces. This latter behavior was observed in

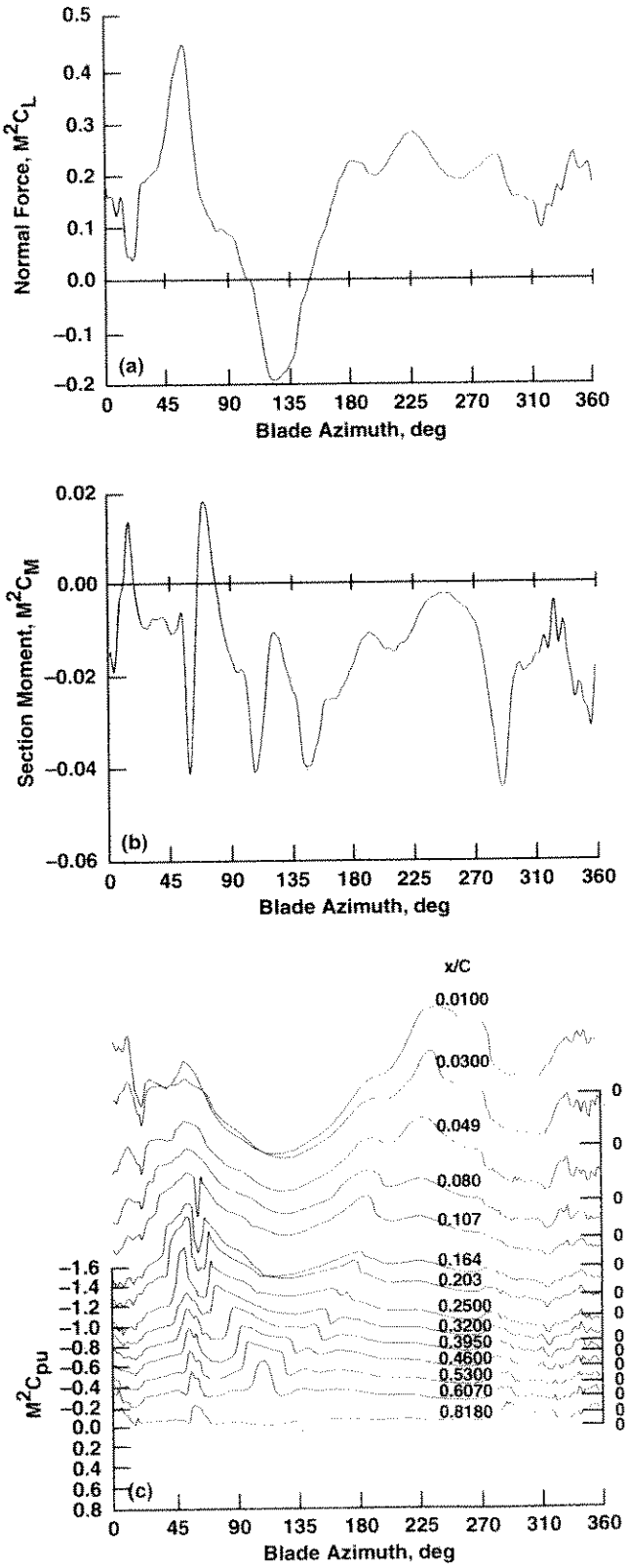

Figure 14. (a) Section normal force, (b) section moment, and (c) an offset plot of upper surface pressures *vs* rotor azimuth for $r/R = 0{\cdot}920$, (Cycle 22, Counter 11 679); 0 to 60 harmonics.

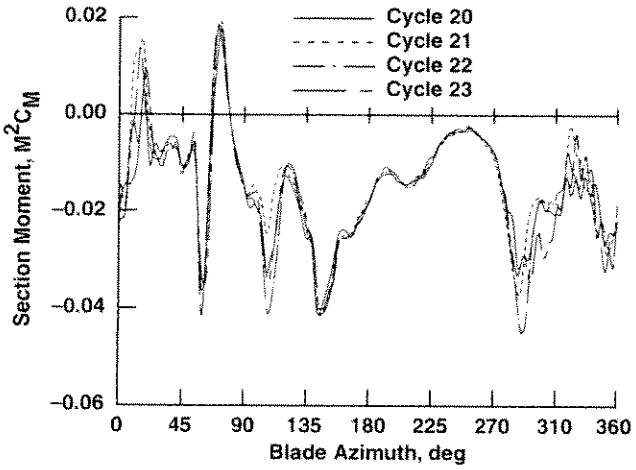

Figure 15. Section moment at 0·92*R vs* rotor azimuth for four adjacent rotor revolution (Counter 11 679); 0 to 60 harmonics.

Ref. 28 for a high speed dive condition, but not for the UTTAS pull-up manoeuvre. Reference 37, after examining both the UTTAS pull-up and the high-speed dive conditions, concluded that the sources of the high torsional loads were two separate phenomena: dynamic stall for the UTTAS manoeuvre and out-of-phase shock motion for the high speed dive case. The diving turn shown here is of particular interest as the measured airloads show that the torsional loads are being caused by both dynamic stall and out of phase shock motion.

The airloads data shown in this paper are clearly a challenge for the analytical prediction codes. Present comprehensive models all employ one or more empirical or semi-empirical dynamic stall models that represent nonlinear, viscous-dominated flows, but none have yet been validated by the kind of three-dimensional aerodynamic loading like that shown here. In addition, the likelihood that any of these methods can predict the detailed effects of unsteady, nonlinear transonic flows in low. New computational fluid dynamic (CFD) codes, on the other hand, should be able to properly characterize the unsteady, nonlinear transonic flows, but do not adequately predict strong viscous effects. In addition, none of these analyses been satisfactorily coupled with dynamic analyses that can represent the blade torsional motions.

The challenge, then, is most simply shown by Fig. 15. Data from four adjacent revolutions of the rotor show that section pitching moments at 0·92*R* are relatively steady. These measured moments are essentially design loads for this aircraft's blades, the rotating controls, and the fixed-system controls. A successful prediction of these loads must properly model dynamic stall and unsteady, nonlinear transonic aerodynamics plus the elastic response of the blade and control system for this steady, trimmed flight condition.

7.0 CONCLUDING REMARKS

The flight test portion of the UH-60A Airloads Program was successfully completed, collecting over 900 in-flight test conditions of a pressure instrumented rotor system. In addition, the aircraft had sufficient instrumentation to clearly identify the aircraft and rotor state and provide useful information for acoustic, loads, vibration, and control research during testing. The test conditions should help to provide information for code validation and increase our understanding of rotor aerodynamics for level flight, manoeuvring flight, acoustics, and flight dynamics. The airloads presented show the detail available for a relatively simple level flight case and a highly complex airloads for a high speed, diving turn.

REFERENCES

1. HOOPER, W.E. The vibratory airloading of helicopter rotors, *Vertica*, 1994, **8**, (2).
2. RABBOTT, J.P. and CHURCHILL, G.B. Experimental investigation of the aerodynamic loading on a helicopter rotor blade in forward flight, NACA RM L56107, 1956.
3. BURPO, F. Measurements of dynamic airloads on a full scale semi rigid rotor, TCREC TR 62–42, 1962.
4. SCHEIMAN, J. A tabulation of helicopter rotor blade differential pressures, stresses, and motions as measured in flight, NASA TM X–952, March 1964.
5. RABBOTT, J.P., LIZAK, A.A. and PAGLINO, V.M. A presentation of measured and calculated full-scale rotor blade aerodynamic and structural loads, USAAVLABS TR 66–31, 1966.
6. RABBOTT, J.P., LIZAK, A.A. and PAGLINO, V.M. Tabulated CH-34 blade surface pressures measured at Nasa/Ames full scale wind tunnel, SER–58399, December 1965.
7. PRUYN, R.R. In-Flight Measurement of rotor blade airloads, bending moments, and motions, together with rotor shaft loads and fuselage vibration, on a tandem rotor helicopter, USAAVLABS TR 67–9A, 1967.
8. BENO, E.A. CH-53A main rotor and stabilizer vibratory airloads and forces, SER 65593, June 1970.
9. SHOCKEY, G.A., COX, C.R. and WILLIAMSON, J.W. AH-1G helicopter aerodynamic and structural loads survey, USAAMRDL TR 76–39, 1977.
10. CROSS, J.L. and WATTS, M. E. Tip aerodynamics and acoustics test, NASA RP 1179, December 1988.
11. CROSS, J. L. and TU, W. Tabulation of data from the tip aerodynamics and acoustics test, NASA TM 102280, November 1990.
12. HEFFERNAN, R.M. and GAUBERT, M. Structural and aerodynamic loads and performance measurements of an SA349/2 helicopter with an advanced geometry rotor, NASA TM 88370, November 1986.
13. BARTSCH, E.A. In-flight measurement and correlation with theory of blade airloads and responses on the XH-51A compound helicopter rotor, Volume I: Measurement and data reduction of airloads and structural loads, USAAVLABS TR 68–28A, 1968.
14. FENAUGHTY, R. and BENO, E. NH-3A vibratory airloads and vibratory rotor loads, SER 611493, January 1970.
15. WATTS, M.E. and CROSS, J.L. The Nasa modern technology rotors program, AIAA 3rd Flight Test Conference, Las Vegas, NV, April 1986.
16. SNYDER, W., CROSS, J. and KUFELD, R. Nasa/Army rotor systems flight research leading to the UH-60A airloads program, AHS Specialists Meeting, Innovation in Rotorcraft Test Technologies, Phoenix, AZ, October 1990.
17. KUFELD, R. and LOSCHKE, P. UH-60 airloads program: status and plans, AIAA Aircraft Design, Systems, and Operations Meeting, Baltimore, MD, September 1991.
18. LIM, J.W. and ANASTASSIADES, T. Correlation of 2GCHAS analysis with experimental data, American Helicopter Society Aeromechanics Specialists Conference, San Francisco, CA, January 1994.
19. LIM, J.W. Analytical investigation of UH-60A flight blade airloads and loads data, American Helicopter Society 51st Annual Forum Proceedings, Fort Worth, TX, May 1995.
20. LORBER, P.F., STAUTER, R.C., and LANDGREBE, A.J. A comprehensive hover test of the airloads and airflow of an extensively instrumented model helicopter rotor, American Helicopter Society 45th Annual Forum, Boston, MA, May 1989.
21. LORBER, P.F. Aerodynamic results of a pressure-instrumented model rotor test at the DNW, *J Ameri Heli Soc*, October 1991, **36**, (4).
22. BUCKANIN, R.M., GOULD, W., LOSIER, P.W., DOWNEY, D.A., LOCKWOOD, R., WEBRE, J.L., HAGAN, J.F., CASON, R.W. and YOUNG, C.J. Rotor systems evaluation, Phase I, AEFA Project No. 85–15, March 1988.
23. CROSS, J., BRILLA, J., KUFELD, R. and BALOUGH, D. The modern rotor aerodynamic limits survey: a report and data survey, NASA TM 4446, October 1993.
24. KUFELD, R., BALOUGH, D., CROSS, J., STUDEBAKER, K., JENNISON, C. and BOUSMAN, W. Flight testing the UH-60A airloads aircraft, American Helicopter Society 50th Annual Forum, Washington DC, May 1994.
25. GAGNON, R. Sub-miniature sensor installation for UH-60A main rotor blade air loads flight test program, International Telemetry Conference, San Diego, CA, 1989.
26. HAMADE, K. and KUFELD, R. Modal analysis of UH-60A instrumented rotor blades, NASA TM 4239, November 1990.

27. BALOUGH, D.L. Estimation of rotor flapping response using blade-mounted accelerometers, American Helicopter Society Aeromechanics Specialists Conference, San Francisco, CA, January 1994.
28. STUDEBAKER, K.F. A survey of hub vibration for the UH-60A airloads research aircraft, American Helicopter Society Aeromechanics Specialists Conference, San Francisco, CA, January 1994.
29. DURNO, J. A., HOWLAND, G.R. and TWOMEY, W. Comparison of Black Hawk shake test results with nastran finite element analysis, American Helicopter Society 43rd Annual Forum Proceedings, St Louis, MO, May 1987.
30. KUFELD, R.M., BOUSMAN, W.G. and CROSS, J.L. A Survey of rotor loads distribution in maneuvering flight, American Helicopter Society Aeromechanics Specialists Conference, San Francisco, CA, January 1994.
31. MUELLER, A.W., CONNER, D.A., RUTLEDGE, C.K. and WILSON, M.R. Full scale flight acoustic results for the UH-60A airloads aircraft, American Helicopter Society Vertical Lift Aircraft Design Conference, San Francisco, CA, January 1995.
32. Operator's manual for army models UH-60A helicopters, Department of the Army, US Army, August 1994, TM 1-1520-237-10.
33. COLEMAN, C.P. and BOUSMAN, W.G. Aerodynamic limitations of the UH-60A rotor, American Helicopter Society Aeromechanics Specialists Conference, San Francisco, CA, January 1994.
34. BOUSMAN, W.G. The response of helicopter rotors to vibratory airloads, *J Ameri Heli Soc*, October 1990, **35**, (4) pp 53-62.
35. TUNG, C., BOUSMAN, W.G. and LOW, S. A Comparison of airloads data between model-scale rotor and full-scale flight test, American Helicopter Society Aeromechanics Technology and Product Design Conference, Bridgeport, CT, October 1995.
36. WILBY, P.G., YOUNG, C. and GRANT, J. An investigation of the influence of fuselage flow field on rotor loads and the effects of vehicle configuration, *Vertica*, 1979, **3**.
37. KUFELD, R.M. and BOUSMAN, W.G., High load conditions measured on an UH-60A in maneuvering flight, American Helicopter Society 51st Annual Forum Proceedings, Fort Worth, TX, May 1995.